Automatic detection of low-backscatter targets in the Arctic using Wide Swath Sentinel-1 imagery

Anca Cristea, A. Malin Johansson, *Member, IEEE,* Anthony P. Doulgeris, *Member, IEEE,* and Camilla Brekke, *Member, IEEE*

***Abstract*—Low backscatter signatures in Synthetic Aperture Radar (SAR) imagery are characteristic to surfaces that are highly smooth and specular reflective of microwave radiation. In the Arctic, these typically represent newly formed sea ice, oil spills, and localized weather phenomena such as low wind or rain cells. The operational monitoring of low backscatter targets can benefit from a stronger integration of freely available SAR imagery from Sentinel-1. We therefore propose a detection method applicable to Sentinel-1 Extra Wide-Swath (EW) SAR scenes. Using intensity values coupled with incidence angle and Noise-Equivalent Sigma Zero (NESZ) information, the image segmentation method is able to detect the low backscatter targets as one segment across sub-swaths. We use the Barents Sea as a test site due to the abundant presence of low backscatter targets with different origins, and of long-term operational monitoring services that help cross-validate our observations. Utilising a large set of scenes acquired in the Barents Sea during the freezing season (November - April), we demonstrate the potential of performing large-scale operational monitoring of local phenomena with low backscatter signatures.**

***Index Terms*—Newly formed sea ice, oil spills, Remote Sensing, SAR, Arctic, Barents Sea, Sentinel-1.**

I. Introduction

THE thinning of sea ice and the reducing sea ice cover [1] imply an increase in sea areas available for maritime traffic in the Arctic [2], where newly formed sea ice and leads provide safe routing for ship traffic and cost-effective passage through ice. Monitoring the shipping routes is important not only for safe shipping, but also out of environmental concerns due to the risk of oil spills. In the Barents Sea, the occurrence of oil slicks is more frequent along the commercial shipping routes or in the vicinity of oil and gas platforms [3]. Awareness of the major locations of oil spills, natural oil seeps [4], newly formed sea ice or other oil spill "lookalikes", structures that have a similar appearance although different origins [5], are important for operational services and their efforts to reduce false alarms. In addition to potentially confusing oil spill detection, new ice formation sites are also of interest for navigation and climate studies. The general thinning of the ice results in an increase in solar energy absorption [6] [7], with expected implications in the energy budget [8], as well as an increase in light transmittance affecting algal growth [9]. In the Barents Sea, most of the sea ice is formed locally, with a fraction imported from the Arctic Basin through the straits between Svalbard and Novaya Zemlya ([10], [11] and [12]).

A. Cristea is with the Norwegian Polar Institute, Tromsø, Norway; A. M. Johansson, A. P. Doulgeris and C. Brekke are with the Department of Physics and Technology, UiT The Arctic University of Norway, 9037 Tromsø, Norway.

New ice formation (frazil, grease and slush) takes place during a large part of the year, both in the marginal ice zone (MIZ) [13] and within sea ice leads.

Operational monitoring of Arctic regions is most reliably performed using passive and active microwave instruments. In [13], Advanced Microwave Scanning Radiometer 2 (AMSR2) data was used to investigate the seasonal evolution of thin ice in the Barents and Kara Seas. AMSR2 has the advantage of being able to accurately capture thin ice areas and provide thickness estimates, albeit at a relatively coarse 5-km resolution. In contrast, Synthetic Aperture Radar (SAR) is more readily used for operational monitoring of sea ice, but cannot provide thickness estimates, although it may be possible to retrieve relative thickness for thin ice, e.g. <30 cm [14], [15]. SAR already has a long history of being used for the operational surveillance of Arctic areas, specifically the detection of ice extent and marine oil spills [16]. In the Barents Sea, the high spatial resolution of SAR systems (Table I) benefits the detection of both oil slicks, as most local oil slicks are between 0.5 and 5 km^2 [3], and of new ice, especially when it occurs along the coastline or in narrow leads. The locations, shapes as well the correlation with sea ice temperature can help distinguish between oil slicks and newly formed sea ice once they are identified, but to the SAR system alone they appear to have similarly low backscatter relative to the background of open water. Oil slicks (mineral/animal/vegetable) and new ice all effectively dampen high frequency waves, thereby creating a smooth surface which reflects electromagnetic radiation and reduces backscatter. Rain cells can produce similar signatures, when rain drops impinging onto the sea surface generate Bragg wave-attenuating turbulence [17]. Certain wave patterns and low wind areas can also present as lookalikes, as they are highly reflective in contrast to the surrounding open water [16]. Signatures of these low backscatter features and their separation in SAR images have been extensively studied since 1990s (e.g. [18] and references therein, [17], [19], [20], [21]). A Bayesian joint segmentation and classification approach has been shown to perform detection of low backscatter leads and open water in Radarsat-2 imagery in [22].

The Extended Wide-Swath (EW) mode of Sentinel-1 has many advantages for operational surveillance: good spatial coverage and temporal resolution (twice daily coverage over the Barents Sea in the HH/HV configuration), as well as the free data policy. However, it can also be difficult to interpret due to corruption by noise artefacts, especially when targeting areas where backscatter values approach the Noise Equivalent Sigma Zero (NESZ), also referred to as the noise

floor. During SAR image formation, the thermal noise inherent to the imaging sensor is inevitably processed together with the raw acquired signal [23]. As a consequence, antenna pattern correction amplifies the noise at the sub-swath edges, resulting in scalloping artefacts that are especially evident in low backscatter regions. The sub-swaths are processed individually and then stitched together, creating additional inter-swath boundary artefacts. NESZ estimates are provided in the product metadata. The typical noise removal procedure consists in simply subtracting these values from the raw intensities, and suppressing any resulting negative values [23]. However, due to imprecision in the NESZ estimates, this approach does not remove the noise patterns completely, an effect which is mainly evident in the cross-polarized channel, which typically has a lower Signal-to-Noise Ratio (SNR) than the co-polarized one. More complex methods that accomplish superior denoising by employing a combination of local and global image adjustments have been designed, with focus on the cross-polarized channel ([24] [25], [26]).

Our contribution specifically targets the mitigation of difficulties raised by noise artefacts in the Sentinel-1 EW mode. We tackle the problem by developing a robust low backscatter target detection algorithm which employs an established clustering-based segmentation framework, and further integrates incidence angle and NESZ information in the segmentation model, for both the co-polarized and cross-polarized channels. The method is tested on a set of 24 scenes containing low backscatter areas with various shapes, sizes and extents, and present all extracted low backscatter segments together with a discussion about their properties. The qualitative evaluation, and comparison with a smaller set of manually segmented slicks, show that the detection of areas with the lowest relative backscatter can be done reliably.

II. Study area and data set

We use dual-polarization Sentinel-1 EW data covering parts of the Barents sea (see Figure 1). The long new ice formation season and high temporal resolution offered by Sentinel-1 makes the Barents Sea an ideal location to test the proposed method. The authors of [13] have identified the peak in new ice formation in the Barents and Kara Seas between October and February, though large inter-annual variations are observed. Here, we focus on the entire freezing season, i.e. from November – April, where the mean temperature is expected to be below -5^{o}C [13]. Images were selected based on their content, i.e. slicks with a variety of shapes, sizes, and positions within the scene. An evaluation by the operational oil spill detection services of SCANEX Moscow has established that the scenes do not contain oil spills, but are a mix of new ice and other lookalikes. Our previous analysis of examples from the same dataset [27] concluded that there is a high likelihood of new ice formation zones being imaged, both close to the shore and in the marginal ice zone. The remaining low backscatter areas are likely low wind fronts. The specifics of the Sentinel-1 images are outlined in Table I (the acronym GRDM stands for "Ground Range Detected Medium resolution") and a list of the images are presented in Table II. In total, 24 scenes from 2017 to 2020 are included in this analysis. Image footprints are shown in Figure 1.

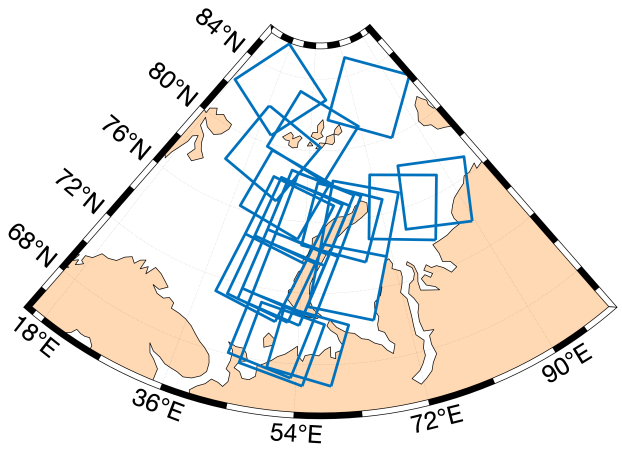

Fig. 1. Outline of the study area, where the blue rectangles show the spatial extent of the included Sentinel-1 images.

TABLE I
SPECIFICS OF THE SENTINEL-1 DATA USED IN THIS STUDY. THE RANGE (RG) AND AZIMUTH (AZ) VALUES ARE GIVEN AS NOMINAL VALUES.

Acquisition mode	EW (GRDM)
Frequency band	C (5.41 GHz)
Polarization mode	HH/HV
Resolution (Rg x Az)	93 m x 87 m
Pixel spacing (Rg x Az)	40 m x 40 m
Swath width	410 km
Incidence angle range	18.9 ^{o}-47.0 ^{o}
Noise Equivalent Sigma Zero (NESZ)	-22 dB

III. Methods

A. Existing Segmentation Framework

The base framework consists in automatic statistical mixture-based clustering applied to polarimetric SAR backscatter and backscatter-derived data. We have previously used complex statistical models that account for textural variations to model the polarimetric data in narrow-swath imagery, such as the K-Wishart [28] and U distributions [29]. As the swaths extend, it becomes necessary to include incidence angle information in order to compensate for the intensity decay from near to far range. The effect of the increased model complexity on the computational load can be mitigated by using a Gaussian approximation for the distribution of log-intensities, which is generally sufficient for the relatively low resolution wide-swath imagery. We have integrated the incidence angle by enforcing non-stationary linearly varying means for the statistical mixture components, parameterized using a decay rate and an intercept [30].

As described in [29] and [30], the clustering problem is solved using an adapted Expectation-Maximization (EM [31]) algorithm. The algorithm is initialized with a single cluster, which is split after model fitting, if the goodness-of-fit criterion

TABLE II
OVERVIEW OF THE SATELLITE SCENES ACQUISITION TIMES AND NUMBER OF IMAGE SAMPLES (PIXELS) USED FOR SEGMENTATION

Scene	Date	Time (UTC)	Sample nb.
# 1	2017/11/27	03:16	12 000
# 2	2017/11/29	03:00	12 000
# 3	2018/04/16	03:47	5 000
# 4	2018/04/16	03:48	5 000
# 5	2018/11/12	02:58	5 000
# 6	2018/11/13	02:00	10 000
# 7	2018/11/14	02:41	5 000
# 8	2018/11/14	02:42	10 000
# 9	2019/01/01	03:30	6 000
# 10	2019/01/01	03:31	3 000
# 11	2019/02/25	03:22	2 500
# 12	2019/02/25	03:23	12 000
# 13	2019/02/25	03:24	2 500
# 14	2019/03/25	03:39	10 000
# 15	2019/03/25	03:40	10 000
# 16	2019/04/01	03:31	7 500
# 17	2019/04/01	03:32	10 000
# 18	2019/10/07	01:28	5 000
# 19	2019/10/07	04:44	2 500
# 20	2019/10/10	05:56	10 000
# 21	2019/10/12	04:03	2 500
# 22	2019/10/13	03:04	7 500
# 23	2019/10/17	04:10	2 500
# 24	2020/02/25	03:30	5 000

(expressed via Pearson's chi-squared test) is not met. The splitting continues until all clusters are considered as good fits to a chosen sensitivity (or confidence level). Finally, hard cluster labels are assigned to all image pixels, according to their associated maximum posterior probabilities. The automatic characteristic of the algorithm refers to its capacity to determine the suitable number of clusters based on the input data, number of samples used for clustering and the chosen confidence level for Pearson's test. A uniformly subsampled subset of the total image pixels are used for clustering, with the dual purpose of reducing the processing time and the number of identifiable clusters (for simplicity). Increasing the confidence level decreases the sensitivity of the test, rendering each class test more tolerant of random variation. The poorest fits will still be separated and hence the major class divisions are still detected, but less distinct clusters (sub-class divisions) are grouped together ([29]). The overall effect will be a reduction in the total number of clusters. We have set the confidence level to 99 % to produce all the results presented in this paper, and adjusted the number of samples for each task (see Table II).

B. Novel Integration of the Variable Noise Floor into the Statistical Model

The approach we propose integrates the nominal noise floor into the statistical model, while allowing its level to be dynamically adjusted during the segmentation process, thus transforming it into a variable noise floor. In [32], the noise

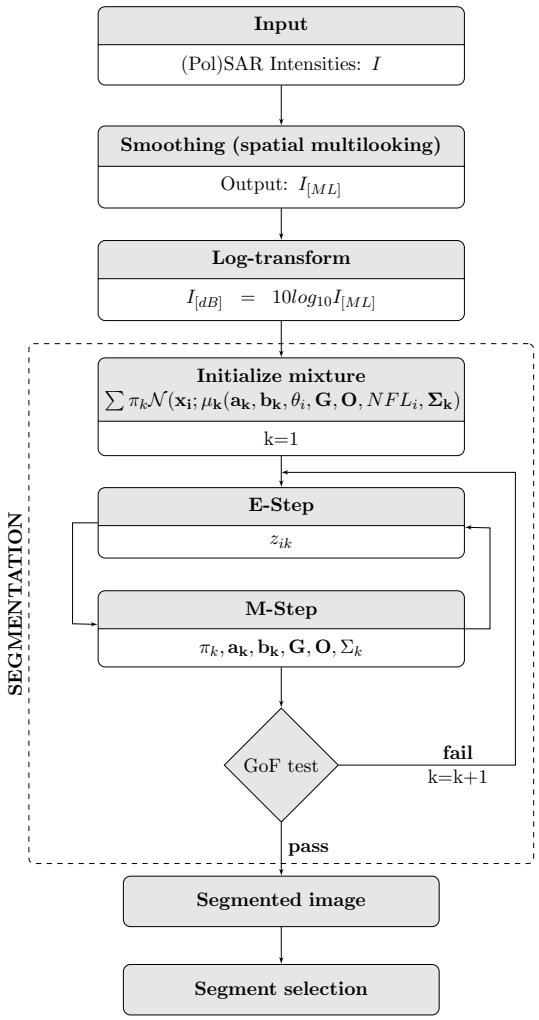

Fig. 2. Schematic representation of the proposed processing steps.

is corrected by adjusting the nominal noise floor considering different gain values for the different sub-swaths, and power-balancing coefficients at the sub-swath boundaries. We have adopted a similar approach in this respect, by using a multiplicative Gain $\mathbf{G}$ and an additive Offset $\mathbf{O}$ for each individual sub-swath.

The distribution of the backscatter coefficients (BSCs, or log-intensities) is modeled by using a statistical mixture of k components (clusters):

$$p_{X,\Theta}(x,\theta) = \sum_{k=1}^{M} \pi_k \frac{1}{(2\pi)^{d/2}|\mathbf{\Sigma}|^{d/2}} e^{-\frac{1}{2}(x-\mu_k)^T \mathbf{\Sigma}^{-1}(x-\mu_k)}, \quad (1)$$

The mixture component mean parameters μ_k vary linearly with the incidence angle value θ_i, $\mathbf{a}_k$ being the intercept and $\mathbf{b}_k$ the decay rate in the log-domain, as already presented in [30]. We introduce the local parameters $\mathbf{G}_{\text{sswi}}$ and $\mathbf{O}_{\text{sswi}}$, which scale the nominal noise floor value NFL_i in sub-swath sswi.

As the noise floor is global and additive in the linear domain [23], it contributes equally to the means of each components:

$$\mu_k(\theta_i, NFL_i) = 10 * log_{10}(10^{(\mathbf{a}_k - \mathbf{b}_k\theta_i)/10} + \mathbf{G}_{sswi} * NFL_i + \mathbf{O}_{sswi}). \quad (2)$$

Note that $\mathbf{a}_k$, $\mathbf{b}_k$, $\mathbf{G}_{\text{sswi}}$ and $\mathbf{O}_{\text{sswi}}$ are d-dimensional vectors for d-dimensional data. In the case of Sentinel-1 dual-polarized data, $d = 2$.

The mixture parameters are estimated by applying the EM algorithm. The EM scheme consists in two stages. In the "Expectation" stage, the a posteriori probabilities that a sample i belongs to a cluster k are obtained as:

$$z_{ik} = \frac{\pi_k \mathcal{N}(\mathbf{x}_i; \mu_k(\theta_i, NFL_i), \mathbf{\Sigma}_k)}{\sum_{j=1}^{M} \pi_j \mathcal{N}(\mathbf{x}_i; \mu_j(\theta_i, NFL_i), \mathbf{\Sigma}_j)}, \quad (3)$$

where $\mathcal{N}(\mathbf{x}_k; \mu_k(\theta_i, NFL_i), \mathbf{\Sigma}_k)$ denotes the Gaussian (Normal) likelihood that the sample $(\mathbf{x}_i, \theta_i)$ belongs to component k. In the second, or "Maximization" stage, both cluster and noise scaling parameters are estimated as follows. The intercept $\mathbf{a}_k$ and decay rate $\mathbf{b}_k$ result from the closed-form expressions:

$$\mathbf{a}_k = \frac{\sum_{i=1}^{n} z_{ik} x_{0i} + \mathbf{b}_k \sum_{i=1}^{n} z_{ik}\theta_i}{\sum_{i=1}^{n} z_{ik}}, \quad (4)$$

$$\mathbf{b}_k = \frac{-\sum_{i=1}^{n} z_{ik}\theta_i x_0 i + \mathbf{a}_k \sum_{i=1}^{n} z_{ik}\theta_i}{\sum_{i=1}^{n} z_{ik}\theta_i^2}, \quad (5)$$

where the "denoised" values $\mathbf{x}_{0i}$ result from subtracting the adjusted noise floor $\mathbf{G}_{sswi} * NFL_i + \mathbf{O}_{sswi}$ from the original linear-domain signal intensities, then converting to decibels:

$$\mathbf{x}_{0i} = 10log_{10}(10^{\mathbf{x_i}/10} - \mathbf{G}_{sswi} * NFL_i - \mathbf{O}_{sswi}) \quad (6)$$

The scaling factor $\mathbf{G}_{sswi}$ and offset $\mathbf{O}_{sswi}$ of the variable noise floor profile are then estimated by solving:

$$\underset{G_{sswi}, O_{sswi}}{\operatorname{argmin}} \sum_{i=1}^{N}\sum_{k=1}^{M}(z_{ik}(\mathbf{x}_i - \mu_k)^2) \quad (7)$$

for each of the 5 sub-swaths, considering μ_k from Eq. 2. The equation can be solved by using a built-in solver, and enforcing numerical constraints. For our MATLAB implementation, we used the built-in optimizer *fmincon*. The parameter bounds for the each of the sub-swaths were determined empirically for consistent performance across the dataset (see Table III). In addition, a positivity constraint was applied, to ensure that the linear-domain intensity values $10^{x_{0i}/10} > 0$.

Finally, the cluster covariances are estimated by applying the classical covariance estimator considering the component means μ_k:

$$\mathbf{\Sigma_k} = \frac{\sum_{i=1}^{n} z_{ik}(\mathbf{x_i} - \mu_\mathbf{k})(\mathbf{x_i} - \mu_\mathbf{k})^T}{\sum_{i=1}^{n} z_{ik}}. \quad (8)$$

One can see that, in contrast to a denoising approach, the proposed approach does not apply any correction to the original data, thus eliminating associated errors. The main source of error is instead represented by deviations of the real data distribution from the assumed model.

TABLE III
OPTIMIZATION BOUNDS FOR G AND O.

G	upper	HH	1.45	1.55	1.45	1.45	1.45
		HV	1.55	1.45	1.45	1.45	1.45
	lower	HH	0.55	0.75	0.75	0.75	0.45
		HV	0.75	0.75	0.65	0.75	0.75
O	upper	HH	0.005	0.005	0.005	0.005	0.005
		HV	0.005	0.005	0.005	0.005	0.005
	lower	HH	-0.0025	-0.0025	-0.0025	-0.0025	-0.0025
		HV	-0.0025	-0.0025	-0.0025	-0.0025	-0.0025

C. Segment selection

Post segmentation, the segment with the lowest intensity at incidence angle $\theta = 32^\circ$ is selected as the dark feature. The reference value of 32° was chosen to be mid-range in order to ensure consistency between images. Morphological erosion is then performed on the extracted dark feature in order to remove small-sized clustering artefacts. A disk-shaped structuring element with a diameter of 1 pixel was used to produce the results.

IV. PERFORMANCE ASSESSMENT AND ANALYSIS OF DETECTED TARGETS

A. Performance gain from integrating the Variable Noise Floor

The goal of the proposed method ("IA+NFL" method) is to extract low backscater targets from noise-corrupted Sentinel-1 EW scenes, while bypassing errors stemming from noise artefacts and preserving integrity across all sub-swaths. We have shown in [27] that the extraction is in some cases also feasible by applying the method published in [30] and briefly described here in section III.A, i.e. Gaussian-mixture based segmentation considering intensity variation with incidence angle ("IA" method), on the co-polarized channel. In this part of the study, we compare the performance of the two methods on two example scenes extracted from the dataset, containing low-backscatter targets of different extents. Scene 24 was selected as an example of relatively small-size targets distributed through the scene, while scene 22 contains an extended target stretching over the entire swath. We use the method published in [30] as reference because, to our knowledge, no methods that deal with similar detection in wide-swath imagery have been published.

The scenes were pre-processed using ESAs Sentinel Application Platform (SNAP) for the extraction of intensity (co-polarized and cross-polarized) and incidence angle information, as well as calibration and land masking. The noise profiles and sub-swath maps were extracted from the original annotation files. For the application of the "IA+NFL" method, the input intensity data only requires calibration. For the application of the "IA" method, it is necessary to perform

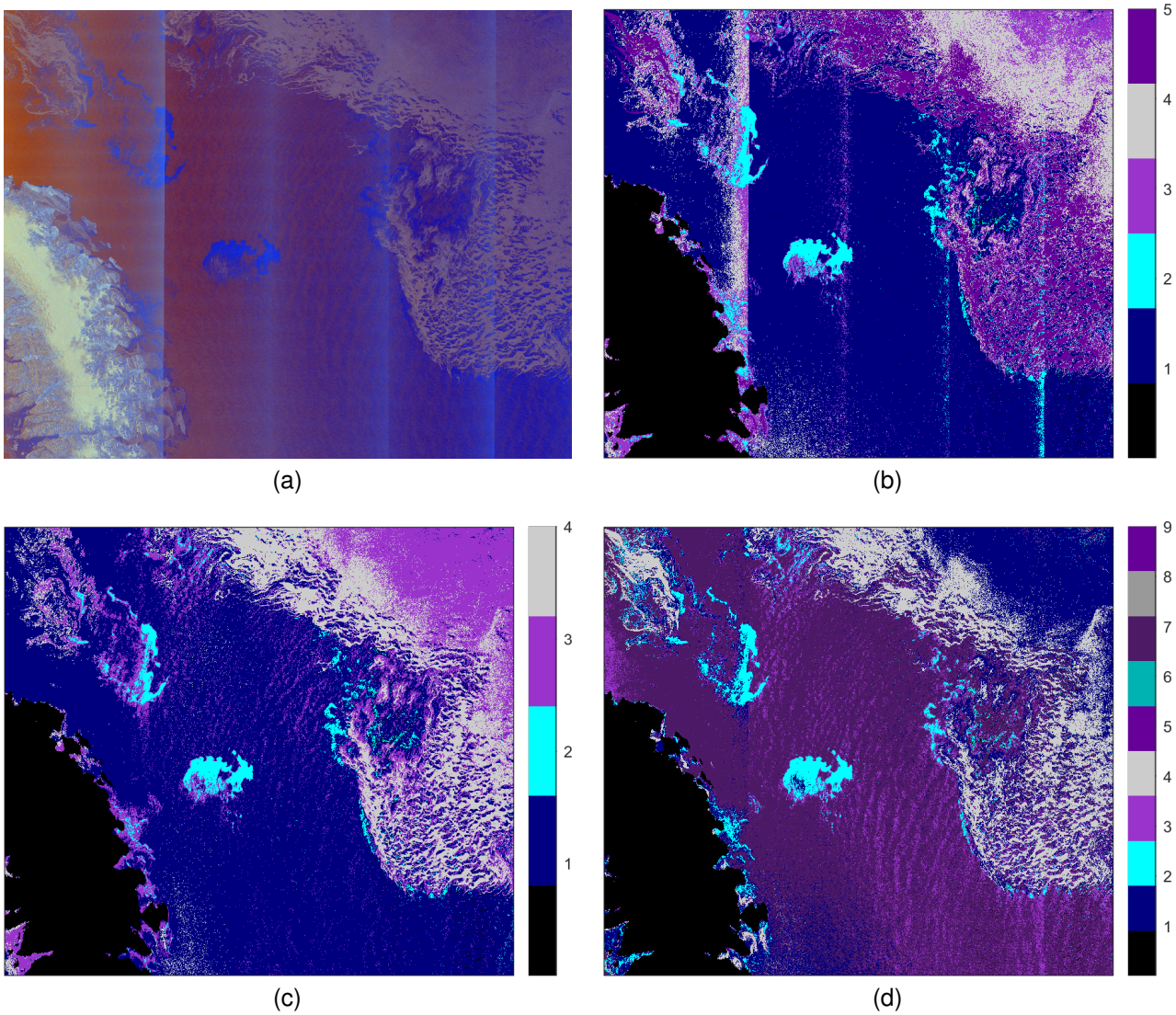

Fig. 3. Scene 24 (a) 3-channel (HH, HV, HV/HH) color composite representation; segmentation result using: (b) IA method on both channels (HH, HV) post-standard noise correction, (c) IA method on the HH channel post-standard noise correction, and (d) IA+NFL method on both channels (HH, HV), without prior noise correction - low backscatter segment is number 2 in all labeled results.

the standard noise correction (via the SNAP software) prior to calibration. Multilooking was applied using an averaging 5x5 pixel window in order to increase radiometric separability, then the image size was reduced by subsampling at a 5x5 rate. Lastly, the intensities and noise profiles were log-transformed, to ensure approximately Gaussian-distributed data and a linear decay with incidence angle.

The assessment overall contains three tests:

- The ”IA” method applied on both data channels (co-polarized and cross-polarized);
- The ”IA” method applied on the co-polarized channel, which is less affected by noise, i.e. the same approach as in [27];
- The proposed ”IA+NFL” method applied on both data channels.

As discussed in the previous subsection, the subsampling rate influences the final number of clusters. The same number of samples (7500) was used for segmentation in this test.

B. Qualitative and quantitative comparison with manually extracted segments

We conducted a comparison with a small set of manually extracted low backscatter targets. The manual extraction has been performed by the operational oil spill detection service of SCANEX Moscow, and precisely delineates the locations of targets with high likelihoods of being newly formed ice, or other oil spill lookalikes. The identification was based on visual examination of the images, after the absence of oil was confirmed using the semi-automatic approach of [3]. The low backscatter targets were clearly identified and delineated down to pixel resolution, thereby enabling a quantitative pixel-to-pixel comparison with the results from the automatic detection algorithm.

The scenes were pre-processed following the same steps as in the previous subsection, with the addition of a geocoding step performed using the SNAP software. A subset of 3 scenes containing low backscatter targets extending over the

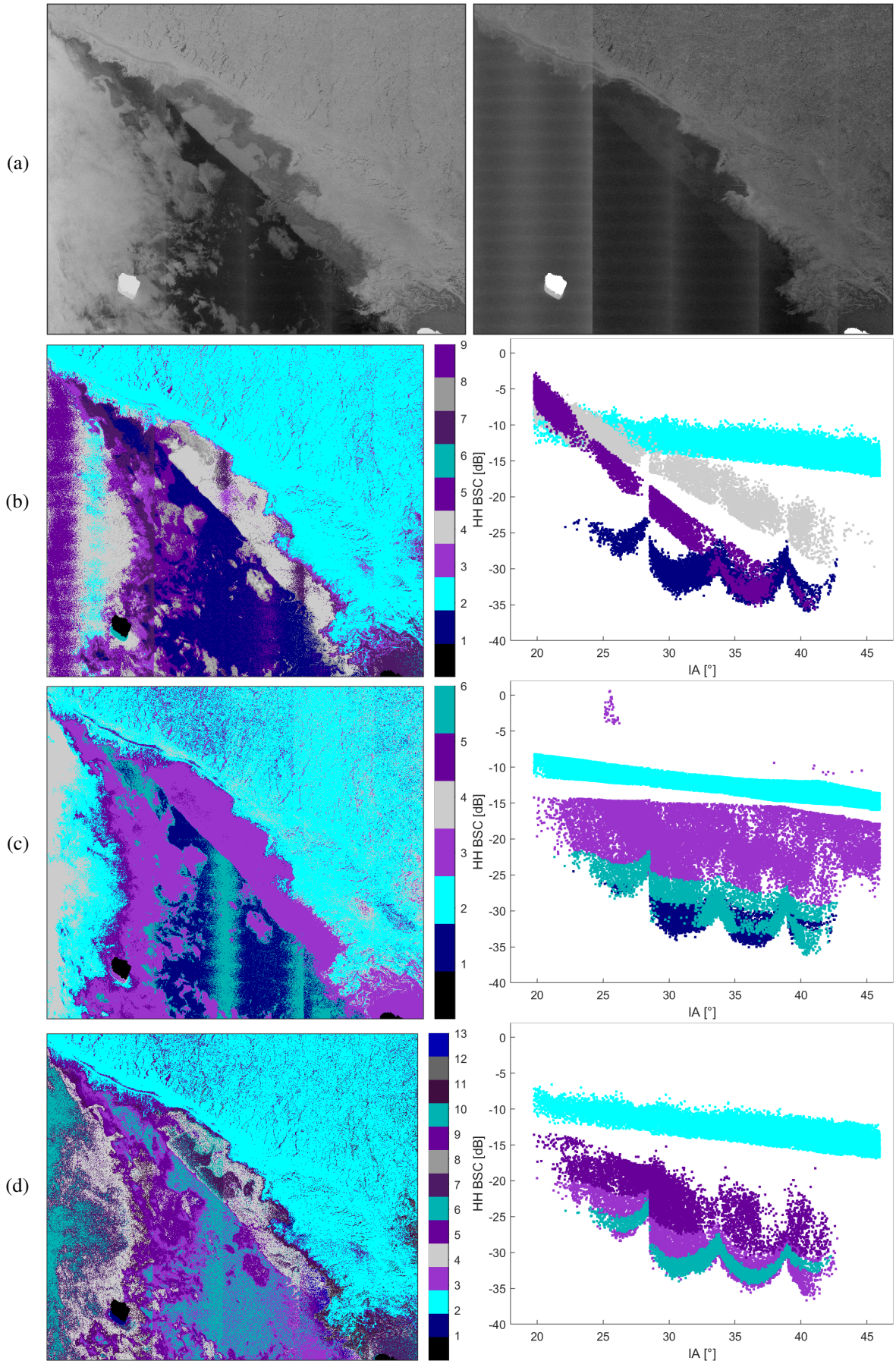

Fig. 4. Scene 22 (a) HH and HV backscatter; segmentation results using: (b) IA method on both channels (HH, HV) post-standard noise correction, (c) IA method on the HH channel post-standard noise correction, and (d) IA+NFL method on both channels (HH, HV), without prior noise correction (low backscatter segment is number 6). The scatter plots show the corresponding distributions of the HH channel BCSs from near to far range, for the most representative segments.

entire swath were selected for the comparison. The number of representative samples used here was slightly higher than in the tests conducted in the previous subsection, proportional to the larger size of the geocoded scenes: 15 000 for scene 1 and scene 2, and 20 000 for scene 7.

C. Evaluation of the output over the entire dataset

The proposed method is applied to the 24 scenes in order to evaluate performance and consistency over a large dataset. Pre-processing was performed as described in Section IV.A.

The selected scenes have almost identical sizes, therefore a simple assumption would be that result consistency could be achieved by using a uniform subsampling rate. However, in practice we observe that scene content also drives the necessity for a variable subsampling rate. We have tested the detection method with variable sample numbers, and empirically settled for the lowest number that would identify the low backscatter segment in each case, and keeping the rest of the scene detail as simple as possible (see values in Table II). We mention that scenes containing low-contrasting targets can benefit from the enhanced radiometric contrast achieved by applying a higher number of looks, but this procedure also carries a risk of enhancing the visibility of noise patterns. The number of samples is the only parameter that we varied in this demonstration.

In addition to the labeled segments, the algorithm also outputs cluster parameters, of which the intercept $\mathbf{a}_k$ (the mean intensity [dB] at $\theta = 0°$) and the decay rate $\mathbf{b}_k$ (intensity decay rate [dB/°]) are examined. The model decay rates are compared with decay rate values computed directly from the image data (raw BSC data used as input, as well as BSC data noise-corrected via SNAP), using the low-backscatter segment masks for selection. Finally, co-polarized BSCs averaged over 1 degree at $20°$, $32°$ and $42°$ (chosen to represent near-range, mid-range and far-range) are also extracted and analyzed.

D. Applicability to the Interferometric Wide (IW) Swath mode

The EW mode of Sentinel-1 is the preferred mode used for environmental surveillance of the Arctic Ocean due to its good spatial and temporal coverage of the area. Imaging of Arctic-adjacent areas is possible with freely available imagery from the same sensor, in the Interferometric Wide-Swath (IW) mode. The IW mode imagery is constructed using a very similar procedure to the EW mode, i.e. by stitching together sub-swaths (3 instead of 5) with curved noise profiles. In the IW mode, the incidence angle range is narrower (approx. 30 to 45°), the resolution is finer (20x22 m for the High resolution Ground Range Detected imagery used here) and the swath width is 250 km. One of the main uses for this mode is oil spill detection, which is why much of the IW imagery is acquired in the VV/VH mode. Different applications are also possible further south, therefore the sought-after targets may be different (for example, coastal erosion can be monitored using this type of imagery [33]), but we show that they can easily be detected using the proposed method if they have low-backscatter signatures.

We present a detection example on an IW scene. The image has been acquired over a frozen up Hudson Strait on 2018/03/06, and contains sea ice, open water and leads (Figure 9). The lead is another type of ocean surface area that can be characterized by low backscatter, as can the open water as observed here. The scene has been processed identically to the EW images, and 12 500 samples were used for segmentation. The constraints for the G and O parameters were kept as in Table III (for sub-swaths 1-3). A finer adjustment of the values is possible, but has not been thoroughly investigated for this mode.

V. Results and discussion

A. Performance gain from integrating the Variable Noise Floor

The full segmentation results of the two sets of tests are shown in Fig. 3 and Fig. 4.

A simple visual examination makes the advantages of the proposed method over the reference method clear when both data channels are used, in both examples: inter-swath boundaries are largely eliminated, and, most importantly, these boundaries are no longer included in the same segment as the areas of interest (in Fig. 3 (b), notice the boundary between sub-swaths 4/5). Segment continuity is preserved across the entire image. Scene 24 presents an example of distributed or "patchy" low backscatter target that is identified both by applying the "IA" method on the co-polarized channel and by applying the proposed "IA+NFL" method on the full dataset. In this example, the segmentation results are overall very similar, with subscene (Fig. 3 (d)) showing small improvements over (Fig. 3 (c)) in terms of ocean detail level and open water/sea ice ambiguities.

Scene 22 contains an example where the benefit of the proposed method over the reference one is evident. Fig. 4 (c) shows how the low backscatter area is not captured accurately when using the co-polarized channel alone. This can be explained by the extent of the target. Low backscatter values lie close to the noise floor, and may therefore not be captured accurately by a model that does not consider the noise floor shape. For a small area, the deviation from the model may not prove to be significant at the targeted level of detail, but as the area size increases, so does the effect of the noise floor. The final result highlights the advantage of considering both channels and incorporating the noise floor (Fig. 4 (d)). Some residual artefacts are still visible at the boundaries between sub-swaths 1/2, and 2/3, respectively, but the integrity of the segment is preserved. Increasing the radiometric contrast (by increasing multilooking) or increasing the desired level of detail of the segmentation (by using more samples) would enhance the likelihood of this scenario also occurring in the case of less extended targets. The plots adjacent to the segmentation results show the co-polarized (HH) BSC distribution from near to far range in each case. For visual clarity, only the most representative segments are included. The plots show how the IA method encounters challenges in relatively low-backscatter areas of the image, where the BSC values more closely follow the oscillating shape of the noise floor, thus risking oversplitting along absolute value boundaries.

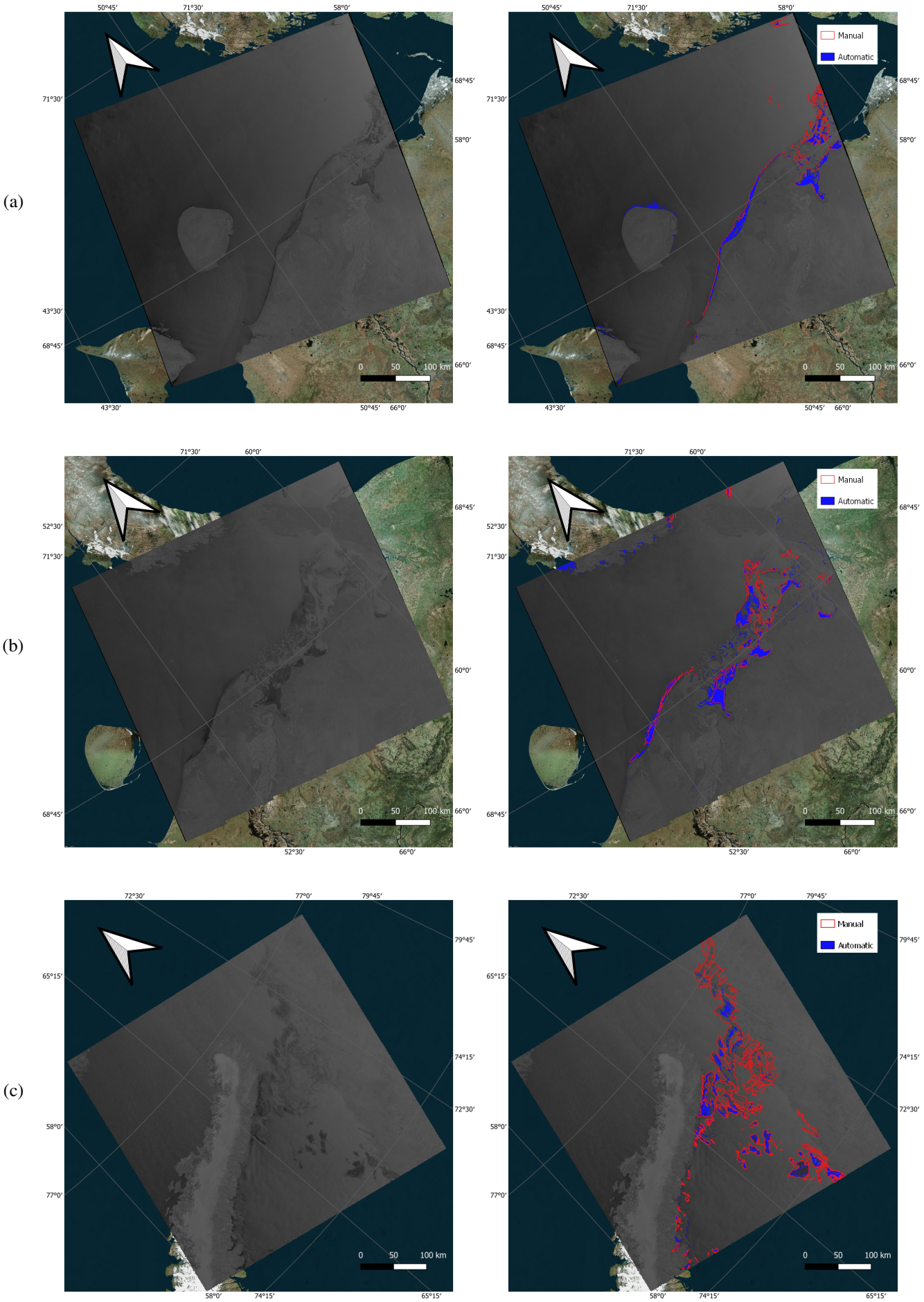

Fig. 5. Segments extracted manually and automatically using the proposed method. Scenes: (a) 1 (b) 2 (c) 7.

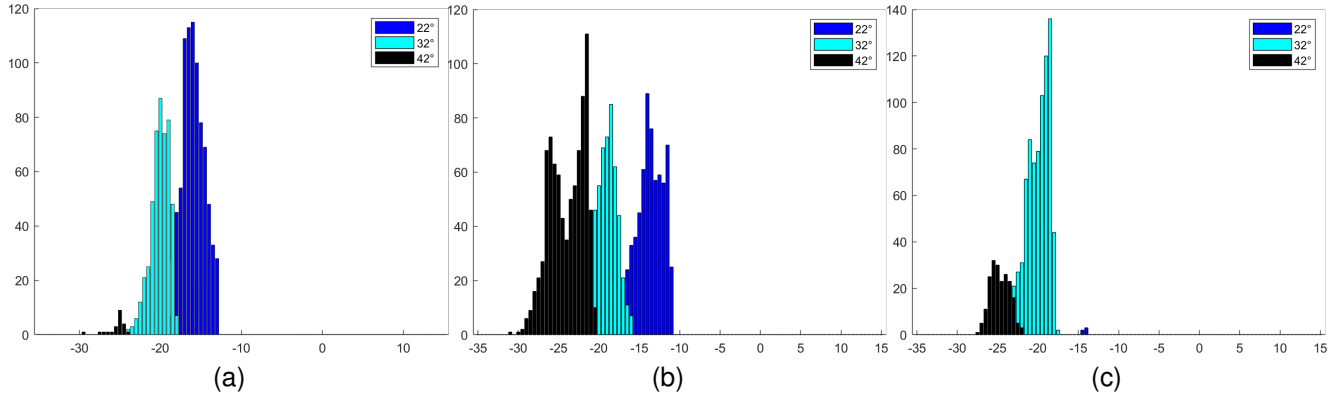

Fig. 6. Extracted low backscatter segments and histogram counts for corresponding BSC values (HH channel) at 22 ^{o}, 32 ^{o}, 42 ^{o}. Scenes (a) 1 (b) 2 (c) 7.

B. Qualitative and quantitative comparison with manually extracted segments

Figure 5 shows the 3 example scenes, highlighting overlaps as well as differences between the automatic and manual selections. The automatically detected segments appear clearly delineated and follow the outlines of the manually extracted segments used as reference. Differences arise in areas where the overall intensity of the backscatter varies, bringing back into discussion the issue of how the targets are defined. The operational oil detection service appears to have a broader definition of the ”low backscatter targets”, which includes the low backscatter regions detected by the proposed method, as well as surrounding brighter areas. Indeed, the automatically extracted segments only cover the darkest image pixels, which is congruent with the model. Quantitatively, the overlaps for scenes 1, 2 and 7 presented in Fig. 5 are of 48%, 56% and 20%, respectively (as a proportion of the manual segment). The smaller overlap registered in the case of scene 7 shows that detection of such targets may prove difficult when the backscatter values vary within the area of interest, as the lighter areas are not easy to capture in a separate segment, i.e they are not ”seen” as one distinct target by the algorithm. It is worth exploring strategies for merging the original target segment with a higher-backscatter segment in a carefully defined neighborhood of the former.

We have observed that variations in the confidence level of the statistical goodness-of-fit test do not produce significant changes in the detected low backscatter segments, and consequently in the overlap percentages, considering the low sample numbers used here. The contrast between low backscatter targets and their neighbors is sufficiently strong for these to count as major class divisions at confidence level values over 90%. However, if the number of samples is increased substantially, the segmentation problem becomes more complex, which often determines the over-splitting of the segment of interest. The number of image samples should therefore be chosen carefully upon implementation in an operational setting, as it carries more weight for the end result.

C. Evaluation of the output over the entire dataset

Low backscatter segments extracted from the 24 scenes are shown in the Appendix. Overall, the observations are similar to those presented in subsection V.A. The segments are continuous across the image and are largely unaffected by the sub-swath boundary discontinuities (including the boundary with the first sub-swath, which presents the largest offset from its neighbor). The intensities of low backscatter targets follow the noise floor closely and are the easiest to separate in the images, once the noise floor is adjusted to even an approximately correct level (since we do not know the actual correct level). Essentially, in many cases we are separating a target whose signature is pure noise. The boundaries become problematic mostly over extended open water areas (calm or wind-roughened), likely due to more significant deviations from the linear approximation of the intensity decay with incidence angle, as in Figures 4 and 10 (c),(g).

Fig. 6 shows the co-polarized BSC value distribution of the low backscatter segments extracted from scenes 1, 2 and 7 (also see Fig.5), in near-range, mid-range and far-range, in intervals of 1° centered at 20°, 32° and 42°, respectively. The distributions are centered around progressively lower values, as expected, and present considerable overlap, even with gaps of 10° between the interval centers. The distribution of BSC values at 42° for scene 2 is bimodal, which may seem to contradict the Gaussian model assumption. However, the cluster parameters resulting from solving the Gaussian mixture are estimated only from the representative samples. The majority of image samples are classified into the most similar cluster, therefore the final classification may contain mixtures.

Figures 7 and 8 show an overview of co-polarized decay rate and BSC values extracted from the detected low backscatter segments. The information is somewhat complementary, as it allows the reader to observe the correspondence between decay rate values and evolution of mean intensities at different incidence angles. Results in Fig. 10, Fig. 11 and Fig. 12 show all low backscatter segments extracted from the dataset, with the exception of those presented in previous subsections. While the number of samples used in this test (Table II) were slightly different for these scenes, the extents of the extracted

segments in both tests are nearly identical. The extraction of the low backscatter segments was successful in all examples, regardless of their spatial positioning (e.g. in the far range where noise is more prominent, at interswath boundaries, or even narrowly in the mid-range, as in Scene 21 - Fig. 12 (d).)

As the "low backscatter" area is defined relative to its surroundings at the specific position in a scene, flat model decay rates can be estimated, as observed in a few cases (in Fig. 7, scenes 11, 16, 17, 20, 21). Estimates from the raw data can even be negative, as in the case of scenes 20 and 21. We also observe that the decay rates estimated as a model parameter can vary considerably in comparison to those computed directly from the BSC values. The variations originate not only from the modeling, but also from differences between the distribution of the final classified pixels and that of the representative samples used to estimate the model decay rates. Of course, the chance of estimating a reliable model decay rate value increases with the range coverage of the low backscatter areas. The model decay rate values estimated here averaged 0.34 ± 0.21 dB/°, while the ones estimated from the raw or noise-corrected intensities have values that are comparable and on average higher than the model decay rates. The former consistently have slightly lower values (0.52 ± 0.28 dB/°) than the latter (0.54 ± 0.34 dB/°). The relatively large variations registered within the selected sample of 24 scenes suggest the need for a larger dataset in order to increase the reliability of the estimates.

Multiple classification studies report decay rate values estimated on various low backscatter targets, using the same type of imagery. A direct comparison with values estimated in the current study must be done carefully, as we do not perform classification and our results likely include a mixture of target types. However, we conclude that the model decay rates estimated here for the co-polarized channel are close to the model decay rates reported for open water in [30], at $0.39\ dB/°$, and all decay rate values are lower than those estimated for open water at $0.65\ dB/°$ in [34] and at $0.72\ dB/°$ in [35], respectively. Decay rates for young ice classes such as reported in [36] and [35] are typically not higher than $0.23\ dB/°$.

D. Applicability to the Interferometric Wide (IW) Swath mode

Figure 9 shows the selected IW scene and segmentation result. The low backscatter areas identified as leads and open water are comprised in segment 2. Like in the previous examples, the integrity of the segment is preserved across sub-swaths, with no boundary impact on the result. This example serves the purpose of showing that the proposed method can detect targets with low backscatter signatures in the IW mode similarly to the EW mode, with no special requirements for the implementation. Efficient use on a variety of scenes may benefit from a finer tuning of the optimization bounds.

VI. Conclusion

We have presented the outline and results of a project with a twofold purpose, mainly, to develop a reliable method for the detection of low backscatter targets in wide-swath SAR imagery from Sentinel-1 while overcoming the poorly defined, variable and stepped noise floor, and secondarily, to offer an overview of some of the properties of the detected targets, based on a study set collected over the Barents Sea. Our detection method is primarily a segmentation algorithm based on Gaussian mixtures with IA- and NESZ-dependent means, adapted to noise-contaminated SAR scenes. We focused on the Barents Sea as a study area, with a selection of 24 scenes containing various types of targets with low backscatter signatures that represent newly formed sea ice and lookalikes. Application on this dataset has consistently produced segments representing the low backscatter targets, clearly delineated and connected across sub-swaths. These results clearly show potential for operational monitoring of phenomena with low backscatter signatures. Validation has been performed using manually extracted segments provided by oil spill monitoring services, which routinely detect oil spill and their lookalikes in the Barents Sea. The validation shows that our estimates

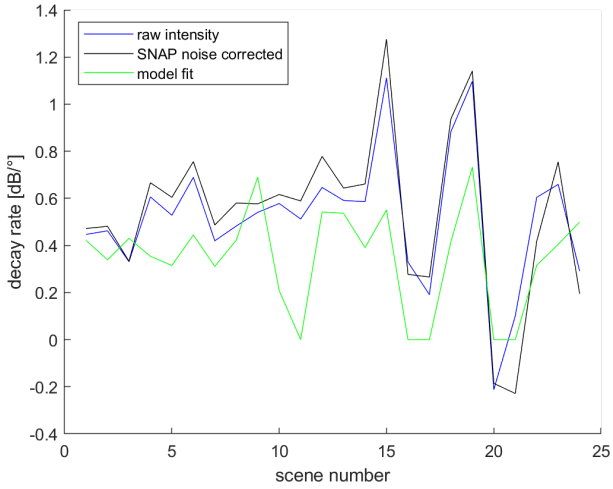

Fig. 7. Decay rate values of the low-backscatter segments in the co-polarized channel, measured on the intensity data before noise correction, after classical noise correction and estimated from the proposed model.

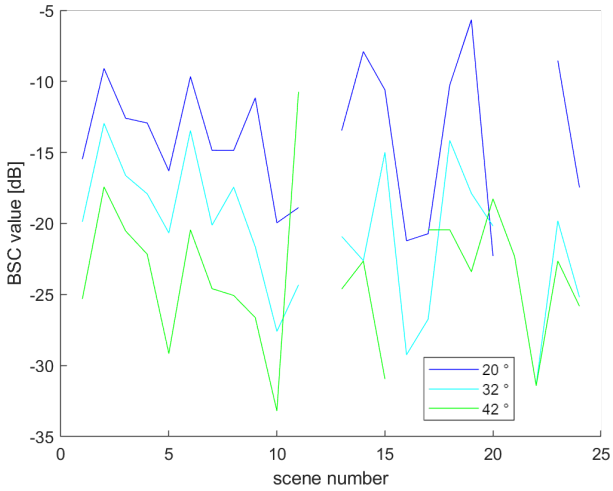

Fig. 8. Mean backscatter values of the low-backscatter segments in the co-polarized channel, measured on the raw (not noise-corrected) intensity data, at 20 ^{o}, 32 ^{o}, 42 ^{o}.

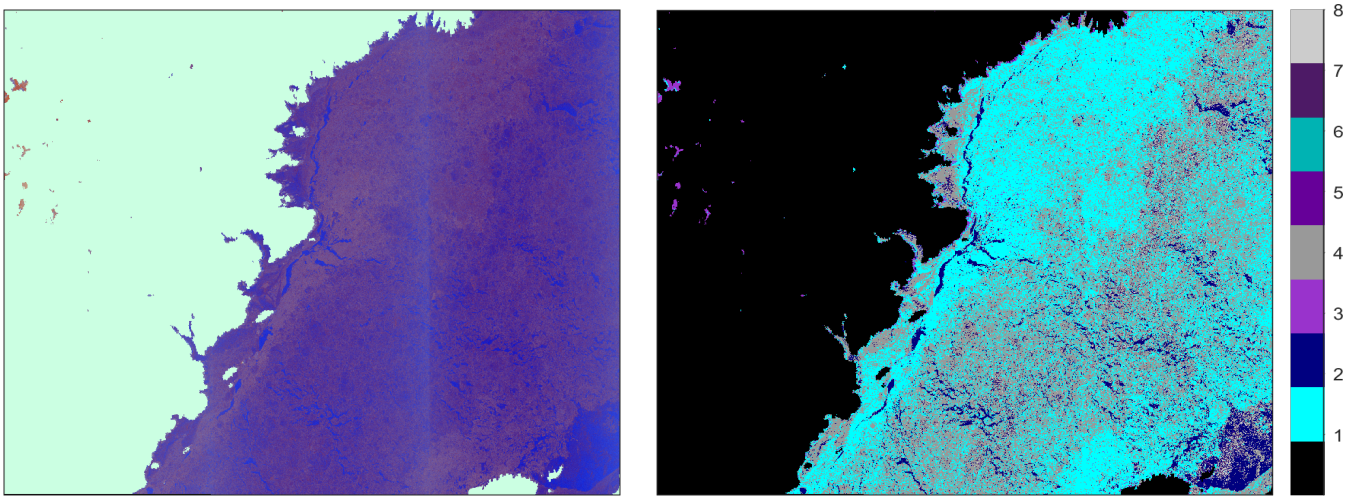

Fig. 9. Application on IW mode (a) 3-channel (HH, HV, HV/HH) color composite representation; (b) segmentation result the IA+NFL method on both channels (VV, VH), without prior noise correction. Black - Landmask. Low backscatter segment is number 2.

essentially capture the areas of interest, but are more conservative than those of the operational service, as they strictly cover the scene areas with the lowest intensity values.

The method shows promise as a general segmentation approach not restricted to low backscatter targets, but requires further development and testing in different conditions before clear conclusions are made. Comparison with other dynamic noise correction methods proposed for the cross-polarized Sentinel-1 EW mode data also constitutes potentially interesting research, although we expect the proposed method to outperform them in the cases of extended low backscatter areas affected by noise in the co-polarized channel. The classification of the detected segments represents the next step, and will require the exploration of multimodal data such as passive microwave, dual- and quad-polarized SAR data. Examples of classification approaches for low backscatter features into oil spills or lookalikes post-detection are summarized in [19]. Features included in the classification are not only related to backscatter levels, but also to the shapes, sizes and locations of the targets. We are also investigating the adaptation of the current method to a supervised approach, where the estimation of the noise balancing coefficients would be done on training areas representing single classes.

ACKNOWLEDGMENTS

The authors wish to thank N. A. Filimonova from the SCANEX Group, Operational monitoring department, Moscow, Russia and D. V. Ivonin from the Shirshov Institute of Oceanology RAS, Moscow, Russia for providing the manually detected segments used for comparison. This work has been funded by CIRFA partners and the Research Council of Norway (RCN grant no. 237906).

APPENDIX
EXTRACTED SEGMENTS

Figures 10, 11 and 12 show the low backscatter segments extracted from the dataset (except scenes 1, 2, 7, 22, 24, which were presented and discussed in detail in previous sections and figures).

REFERENCES

[1] J. Stroeve, T. Markus, W. Meier, and J. Miller, "The Arctic's rapidly shrinking sea ice cover: A research synthesis," *Climatic Change*, vol. 110, pp. 1005–1027, 2012.

[2] S. R. Stephenson, L. C. Smith, L. W. Brigham, and J. A. Agnew, "Projected 21st-century changes to arctic marine access," *Climatic Change*, vol. 118, no. 3-4, pp. 885–899, 2013.

[3] A. Ivanov, N. Filimonova, A. Kucheiko, N. Evtushenko, and N. Terleeva, "Oil spills in the Barents Sea based on satellite monitoring using SAR: spatial distribution and main sources," *International Journal of Remote Sensing*, vol. 39, no. 13, pp. 4484–4498, 2017.

[4] R. Lutz, P. Klitzke, P. Weniger, M. Blumenberg, D. Franke, L. Reinhardt, A. Ehrhardt, and K. Berglar, "Basin and petroleum systems modelling in the northern norwegian barents sea," *Marine and Petroleum Geology*, vol. 130, p. 105128, 2021. [Online]. Available: https://www.sciencedirect.com/science/article/pii/S0264817221002312

[5] W. Alpers, B. Holt, and K. Zeng, "Oil spill detection by imaging radars: challenges and pitfalls," *Remote Sensing of Environment*, vol. 201, pp. 133–147, 2017.

[6] M. Nicolaus, C. Katlein, J. Maslanik, and S. Hendricks, "Changes in arctic sea ice result in increasing light transmittance and absorption," *Geophysical Research Letters*, vol. 39, no. 24, 2012. [Online]. Available: https://agupubs.onlinelibrary.wiley.com/doi/abs/10.1029/2012GL053738

[7] D. Perovich, B. Light, and S. Dickinson, "Changing ice and changing light: trends in solar heat input to the upper arctic ocean from 1988 to 2014," *Annals of Glaciology*, vol. 61, no. 83, p. 401–407, 2020.

[8] V. P. Walden, S. R. Hudson, L. Cohen, S. Y. Murphy, and M. A. Granskog, "Atmospheric components of the surface energy budget over young sea ice: Results from the N-ICE2015 campaign," *Journal of Geophysical Research: Atmospheres*, vol. 122, no. 16, pp. 8427–8446, 2017. [Online]. Available: https://agupubs.onlinelibrary.wiley.com/doi/abs/10.1002/2016JD026091

[9] H. M. Kauko, T. Taskjelle, P. Assmy, A. K. Pavlov, C. J. Mundy, P. Duarte, M. Fernández-Méndez, L. M. Olsen, S. R. Hudson, G. Johnsen, A. Elliott, F. Wang, and M. A. Granskog, "Windows in arctic sea ice: Light transmission and ice algae in a refrozen lead," *Journal of Geophysical Research: Biogeosciences*, vol. 122, no. 6, pp. 1486–1505, 2017. [Online]. Available: https://agupubs.onlinelibrary.wiley.com/doi/abs/10.1002/2016JG003626

[10] T. Vinje and A. S. Kvambekk, "Barents sea drift ice characteristics," *Polar Research*, vol. 10, no. 59-68, 1991.

[11] S. Kern, Y. Chen, D. Stammer, and G. Spreen, "The sea-ice compactness in the Greenland and Barents Seas during 1979-2003: changes and links to the surface air flow," *Annals of Glaciology*, vol. 44, no. 30-36, 2006.

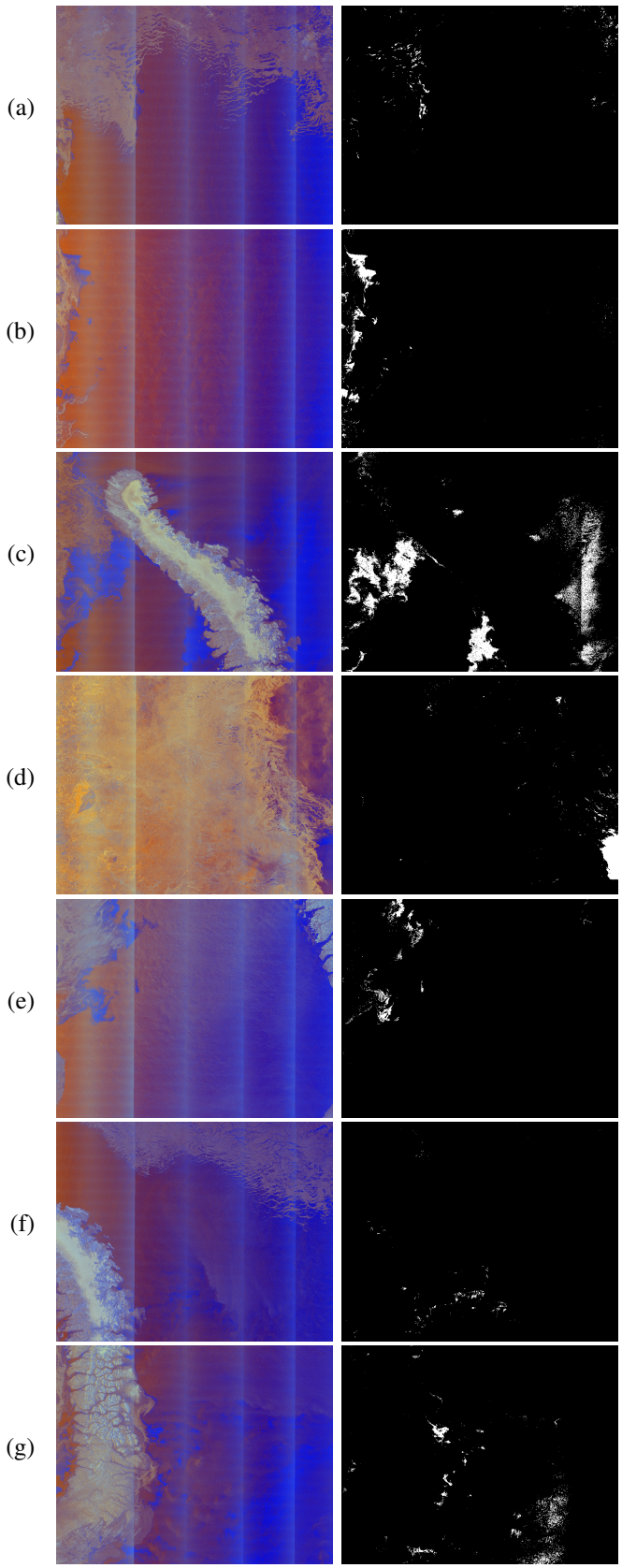

Fig. 10. 3-channel (HH, HV, HV/HH) color composite representations and extracted slick from scenes: (a) 3 (b) 4 (c) 5 (d) 6 (e) 8 (f) 9 (g) 10.

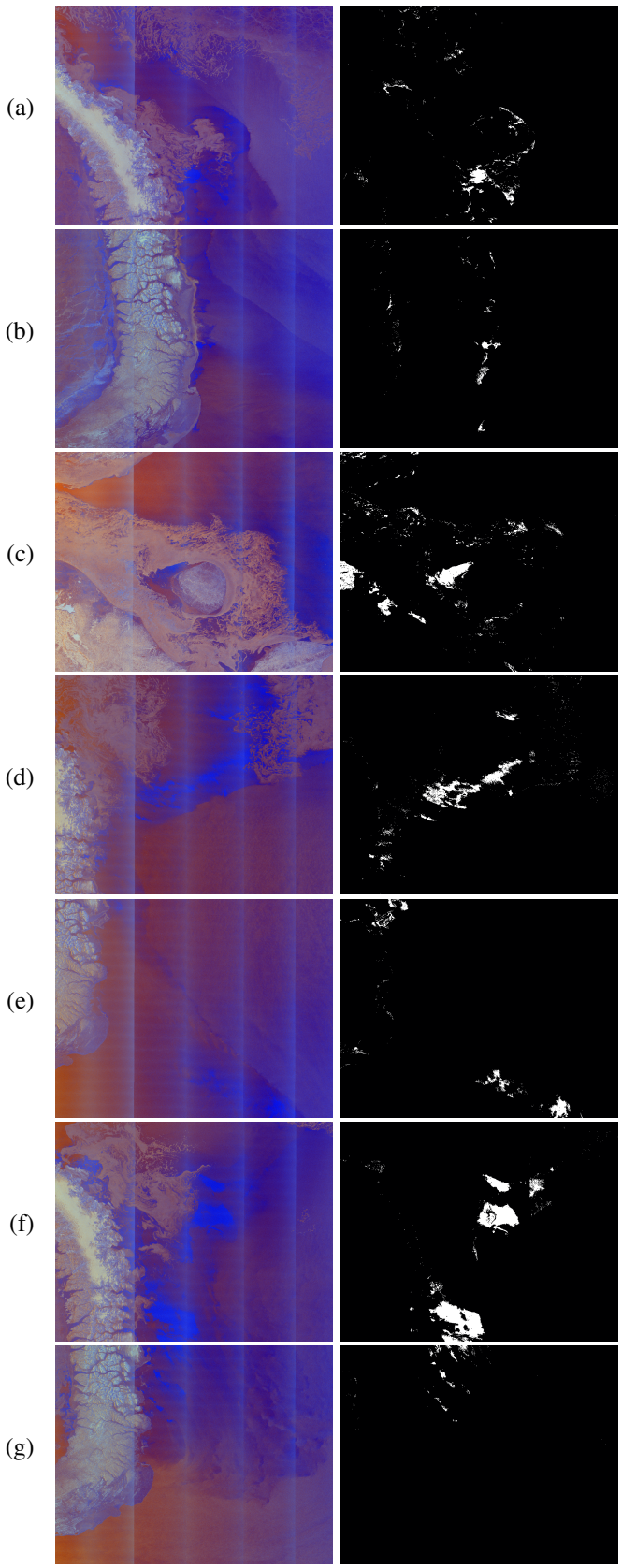

Fig. 11. 3-channel (HH, HV, HV/HH) color composite representations and extracted slick from scenes: (a) 11 (b) 12 (c) 13 (d) 14 (e) 15 (f) 16 (g) 17.

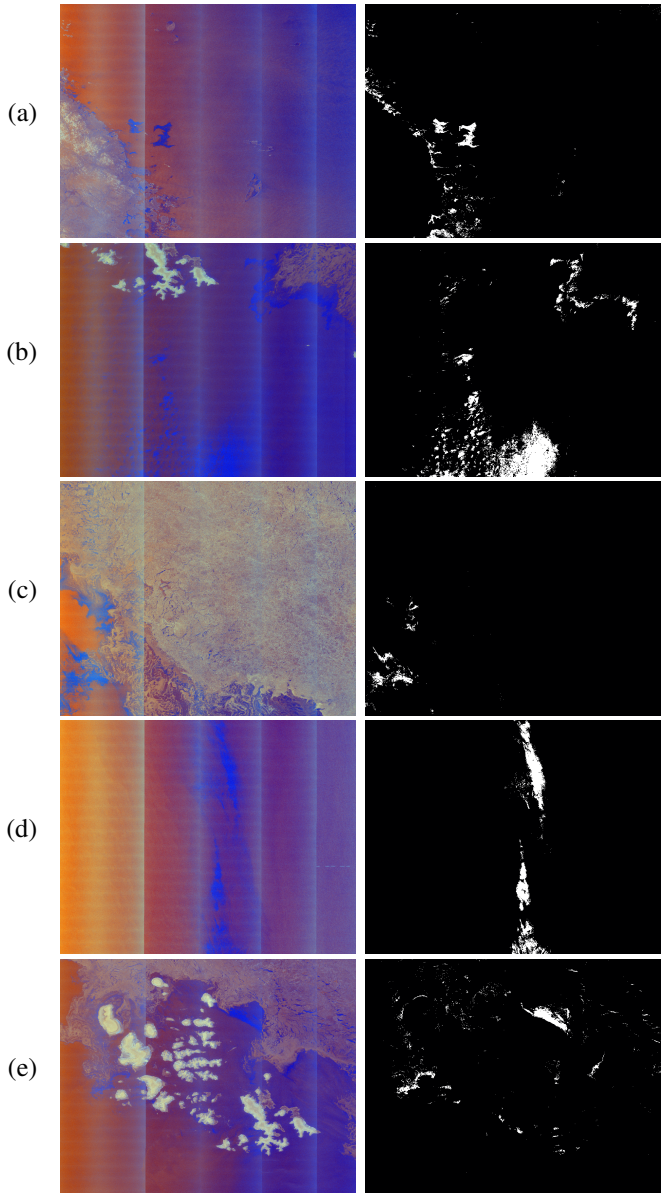

Fig. 12. 3-channel (HH, HV, HV/HH) color composite representations and extracted slick from scenes: (a) 18 (b) 19 (c) 20 (d) 21 (e) 23.

[12] O. Pavlova, V. Pavlov, and S. Gerland, "The impact of winds and sea surface temperatures on the Barents Sea ice extent, a statistical approach," *Journal of Marine Systems*, vol. 130, no. 248-255, 2014.

[13] M. Mäkynen and M. Similä, "Thin ice detection in the Barents and Kara seas using AMSR2 high-frequency radiometer data," *IEEE Transactions on Geoscience and Remote Sensing*, vol. 57, no. 10, 2019.

[14] A. M. Johansson, J. A. King, A. P. Doulgeris, S. Gerland, S. Singha, G. Spreen, and T. Busche, "Combined observations of Arctic sea ice with near-coincident colocated X-band, C-band, and L-band SAR satellite remote sensing and helicopter-borne measurements," *Journal of Geophysical Research: Oceans*, vol. 122, no. 1, pp. 669–691, 2017. [Online]. Available: http://dx.doi.org/10.1002/2016JC012273

[15] R. G. Onstott, *SAR and Scatterometer Signatures of Sea Ice*. American Geophysical Union, 1992, pp. 73–104. [Online]. Available: http://dx.doi.org/10.1029/GM068p0073

[16] C. Brekke and A. Solberg, "Oil spill detection by satellite remote sensing," *Remote Sensing of Environment*, vol. 95, pp. 1–13, 2005.

[17] W. Alpers, B. Zhang, A. Mouche, K. Zeng, and P. W. Chan, "Rain footprints on C-band synthetic aperture radar images of the ocean - Revisited," *Remote Sensing of Environment*, vol. 187, pp. 169–185, 2016. [Online]. Available: https://www.sciencedirect.com/science/article/pii/S003442571630387X

[18] M. Gade, W. Alpers, H. Hühnerfuss, V. R. Wismann, and P. A. Lange, "On the reduction of the radar backscatter by oceanic surface films: Scatterometer measurements and their theoretical interpretation," *Remote Sensing of Environment*, vol. 66, pp. 52–70, 1998.

[19] K. N. Topouzelis, "Oil spill detection by sar images: Dark formation detection, feature extraction and classification algorithms," *Sensors (Basel)*, vol. 8, no. 10, pp. 6642–6659, 2008.

[20] K. Topouzelis and D. Kitsiou, "Detection and classification of mesoscale atmospheric phenomena above sea in sar imagery," *Remote Sensing of Environment*, vol. 160, pp. 263–272, 2015. [Online]. Available: https://www.sciencedirect.com/science/article/pii/S0034425715000528

[21] A. M. Johansson, C. Brekke, G. Spreen, and J. A. King, "X-, C-, and L-band SAR signatures of newly formed sea ice in Arctic leads during winter and spring," *Remote Sensing of Environment*, vol. 204, no. Supplement C, pp. 162 – 180, 2018. [Online]. Available: http://www.sciencedirect.com/science/article/pii/S0034425717304960

[22] Q. Yu and D. A. Clausi, "Sar sea-ice image analysis based on iterative region growing using semantics," *IEEE Transactions on Geoscience and Remote Sensing*, vol. 45, no. 12, pp. 3919–3931, 2007.

[23] G. Hajduch, N. Miranda, R. Piantanida, P. Meadows, P. Vincent, and N. Franceschi, "S-1 Mission Performance Centre, Thermal Denoising of Products Generated by the S-1 IPF, Issue 1. 1," 2017.

[24] J.-W. Park, J.-S. Won, A. A. Korosov, M. Babiker, and N. Miranda, "Textural Noise Correction for Sentinel-1 TOPSAR Cross-Polarization Channel Images," *IEEE Transactions on Geoscience and Remote Sensing*, vol. 57, no. 6, pp. 4040–4049, 2019.

[25] P. Q. Lee, L. Xu, and D. A. Clausi, "Sentinel-1 additive noise removal from cross-polarization extra-wide TOPSAR with dynamic least-squares," *Remote Sensing of Environment*, vol. 248, p. 111982, 2020. [Online]. Available: https://www.sciencedirect.com/science/article/pii/S0034425720303527

[26] Y. Sun and X.-M. Li, "Denoising Sentinel-1 Extra-Wide Mode Cross-Polarization Images Over Sea Ice," *IEEE Transactions on Geoscience and Remote Sensing*, vol. 59, no. 3, pp. 2116–2131, 2021.

[27] A. Cristea, A. M. Johansson, N. A. Filimonova, D. V. Ivonin, N. Hughes, A. P. Doulgeris, and C. Brekke, "Towards Automatic Detection of Dark Features in the Barents Sea using Synthetic Aperture Radar," in *IGARSS 2020 - 2020 IEEE International Geoscience and Remote Sensing Symposium*, 2020, pp. 2455–2458.

[28] A. P. Doulgeris, S. N. Anfinsen, and T. Eltoft, "Automated Non-Gaussian Clustering of Polarimetric Synthetic Aperture Radar Images," *IEEE Transactions on Geoscience and Remote Sensing*, vol. 49, no. 10 PART 1, pp. 3665–3676, 2011.

[29] A. P. Doulgeris, "An Automatic U-Distribution and Markov Random Field Segmentation Algorithm for PolSAR Images," *IEEE Transactions on Geoscience and Remote Sensing*, vol. 53, no. 4, pp. 1819–1827, 2015.

[30] A. Cristea, J. van Houtte, and A. P. Doulgeris, "Integrating Incidence Angle Dependencies Into the Clustering-Based Segmentation of SAR Images," *IEEE Journal of Selected Topics in Applied Earth Observations and Remote Sensing*, vol. 13, pp. 2925–2939, 2020.

[31] A. P. Dempster, N. M. Laird, and D. B. Rubin, "Maximum Likelihood from Incomplete Data via the EM Algorithm," *Journal of the Royal Statistical Society. Series B*, vol. 39, no. 1, pp. 1–38, 1977.

[32] J.-W. Park, A. A. Korosov, M. Babiker, S. Sandven, and J.-S. Won, "Efficient Thermal Noise Removal for Sentinel-1 TOPSAR Cross-Polarization Channel," *IEEE Transactions on Geoscience and Remote Sensing*, vol. 56, no. 3, pp. 1555–1565, 2018.

[33] A. Bartsch, S. Ley, I. Nitze, G. Pointner, and G. Vieira, "Feasibility study for the application of synthetic aperture radar for coastal erosion rate quantification across the arctic," *Frontiers in Environmental Science*, vol. 8, 2020. [Online]. Available: https://www.frontiersin.org/articles/10.3389/fenvs.2020.00143

[34] Park, J.-W. and Korosov, A. A. and Babiker, M. and Won, J.-S. and Hansen, M. W. and Kim, H.-C., "Classification of sea ice types in sentinel-1 synthetic aperture radar images," *The Cryosphere*, vol. 14, no. 8, pp. 2629–2645, 2020. [Online]. Available: https://tc.copernicus.org/articles/14/2629/2020/

[35] J. Lohse, A. P. Doulgeris, and W. Dierking, "Mapping sea-ice types from Sentinel-1 considering the surface-type dependent effect of incidence angle," *Annals of Glaciology*, vol. 61, no. 83, p. 260–270, 2020.

[36] W. Guo, P. Itkin, J. Lohse, M. Johansson, and A. P. Doulgeris, "Cross-platform classification of level and deformed sea ice considering per-class incident angle dependency of backscatter intensity," *The Cryosphere*, vol. 16, no. 1, pp. 237–257, 2022. [Online]. Available: https://tc.copernicus.org/articles/16/237/2022/

Anca Cristea received the B.Sc. degree in applied electronics and M.Sc. degree in image processing from the Politehnica University of Bucharest, Bucharest, Romania, in 2010 and 2012, respectively, and the Ph.D. degree in signal and image processing from the Claude Bernard Lyon 1 University, Villeurbanne, France, in 2015. Her research has previously focused on medical ultrasound imaging, with emphasis on statistical methods for quantitative ultrasound. Currently, she is a Postdoctoral Researcher with The Norwegian Polar Institute in Tromsø, Norway, working on segmentation and classification algorithms for Synthetic Aperture Radar with applications to the cryosphere.

A. Malin Johansson received the M.Sc. degree in physical oceanography from Gothenburg University, Gothenburg, Sweden, in 2005, and the Ph.D. degree in remote sensing from Stockholm University, Stockholm, Sweden, in 2012. She was a Post-Doctoral Researcher with the Radar Remote Sensing Group, Department of Earth and Space Sciences, Chalmers University of Technology, Gothenburg. She joined the Department of Physics and Technology, UiT The Arctic University of Norway, Tromsø, Norway, in 2014, where is she currently an Associate Professor. Her research interest includes multisensor, primarily SAR, remote sensing of sea ice and oil spills.

Anthony P. Doulgeris (S'06–M'12-SM'17) received the B.Sc. degree in physics from The Australian National University, Canberra, Australia, in 1988, the M.Sc. degree and the Ph.D. degree in physics from the Department of Physics and Technology, UiT The Arctic University of Norway, Tromsø, Norway, in 2006, and 2011, respectively.

He joined the Department of Physics and Technology at the UiT The Arctic University of Norway in 2007, and is currently a Professor and head of the Earth Observation group. His research interests focus on developing generic algorithms for remote sensing, pattern recognition and multidimensional statistical modelling, in particular for polarimetric SAR applications in sea ice and glaciers.

Camilla Brekke received the Cand. Mag. (BSc) and Cand. Scient. (MSc), in informatics, and Ph.D. degrees in remote sensing and image analysis from the Department of Informatics, University of Oslo, Oslo, Norway, in 1998, 2001, and 2008, respectively. She is a Professor with the Department of Physics and Technology, UiT The Arctic University of Norway, Tromsø, Norway. Since 2021, she is the Pro-Rector for Research and Development at UiT. Her research interests include Synthetic Aperture Radar and ocean color remote sensing for Arctic and marine applications.